Journal of Alloys and Compounds 524 (2012) 32–37

Contents lists available at SciVerse ScienceDirect

Journal of Alloys and Compounds

journal homepage: www.elsevier.com/locate/jallcom

The constitutive response of three solder materials

Alejandro G. Perez-Bergquist[a,*], Fang Cao[b], Sara J. Perez-Bergquist[a], Mike F. Lopez[a], Carl P. Trujillo[a], Ellen K. Cerreta[a], George T. Gray III[a]

[a] Materials Science and Technology Division, Los Alamos National Laboratory, Mail Stop G755, Los Alamos, NM 87545, USA
[b] Exxon Mobil Research and Engineering Company, Annadale, NJ 08801, USA

ARTICLE INFO

Article history:
Received 9 December 2011
Received in revised form 25 January 2012
Accepted 5 February 2012
Available online 16 February 2012

Keywords:
Solder
Mechanical properties
Microstructure
Temperature dependence
Strain rate sensitivity

ABSTRACT

As increasing worldwide demand for portable consumer electronics drives development of smaller, faster, more powerful electronic devices, components in these devices must become smaller, more precise, and more robust. Often, failure of these devices comes as a result of failure of the package (i.e. when a mobile phone is dropped) and specifically comes as a result of failure of solder interconnects. As a result, stronger more reliable solder materials are needed. In this paper, the constitutive responses of three solder materials (Sn63Pb37, Sn62Pb36Ag2, and Sn96.5Ag3Cu0.5) are analyzed as a function of temperature (−196 °C to 60 °C) and strain rate (10^{-3} to $>10^{3}$ s^{-1}). The lead-free Sn96.5Ag3Cu0.5 possessed the highest yield stress of the three solders at all tested strain rates and temperatures, and all solder microstructures which displayed a mechanical response that was sensitive to temperature exhibited grain coarsening with increasing plastic strain, even at room temperature.

Published by Elsevier B.V.

1. Introduction

Traditionally, solders in consumer electronics have been used as convenient joints and to ensure electrical contact between components, but typically solders were not expected to provide high mechanical strength. Recently, however, there is an enhanced need for electronic devices to survive and function in ever increasing extreme environments. Electronic components are now often asked to perform under conditions of high stress, high strain, or after high strain rate loads have been applied. In addition, these same components may be subjected to large and/or frequent fluctuations in temperature, which can induce high temperature creep fracture and enhanced mechanical and thermal failure in solders [1–3]. At the same time, manufacturers face growing restrictions in the use of leaded solders, as national and local governments, such as the European Union, China, and the state of California, increasingly adopt resolutions prohibiting the addition of lead to consumer electronics [4].

In order to design and implement solders that are both physically robust and environmentally friendly, knowledge of the mechanical properties of various solder materials under a wide range of temperatures and strain rates is required. While there is a well-developed field of study dedicated to the electronic properties of these materials, there has been less work conducted to quantify their mechanical properties and associated microstructural and substructural evolutions after deformation. A factor that complicates characterization of solders is the fact that microstructures of solder materials, both leaded and lead free, change over time. This is due to both the comparatively high homologous temperatures that occur during processing and operation of these components and the thermal mismatches between materials in microelectronic devices [5]. While numerous studies have been performed on the stress–strain behavior [6,7], mechanical behavior [8–10], and microstructure [11–14] of various solder alloys under different testing conditions, due to the large numbers of solder alloys in use, as well as the complications in characterization listed above, much work remains to be done.

In this study, the constitutive behaviors of three solder alloys, Sn63Pb37, Sn62Pb36Ag2, and Sn96.5Ag3Cu0.5, are examined as a function of temperature and strain rate. Sn63Pb37 and Sn62Pb36Ag2 are leaded solders that are commonly used in electronics. Sn63Pb37 is a eutectic solder with a melting point of 183 °C, and Sn62Pb36Ag2 is a silver-alloyed solder with a melting point of 179 °C that possesses both a relatively higher strength and creep resistance [15]. These solders are compared to Sn96.5Ag3Cu0.5, a lead-free solder with a very narrow melting range of 217–218 °C. It has a long history of use in Japanese electronics manufacturing and is recommended for wave and reflow soldering applications [16]. Each solder material is characterized prior to and after testing to understand the substructural evolution of these multi-phase alloy systems and to correlate observed properties with microstructures during loading.

* Corresponding author. Tel.: +1 505 667 1427.
E-mail address: alexpb@lanl.gov (A.G. Perez-Bergquist).

0925-8388/$ – see front matter. Published by Elsevier B.V.
doi:10.1016/j.jallcom.2012.02.049

2. Experimental

The solder materials used in this investigation included industrial purity Sn63Pb37 (S1), Sn62Pb36Ag2 (S2) and Sn96.5Ag3Cu0.5 (S3) in wt%. All three solders were originally bar stock, with S1 being cylindrical with a diameter of 3.175 mm, S2 being an isosceles trapezoid with a height of 10 mm and top and bottom widths of 12.5 mm and 19.75 mm respectively, and S3 being an equilateral triangular prism with side length of 23 mm. Optical microscopy (OM) and scanning electron microscopy (SEM) were used to characterize the as-received microstructure of the three alloys. S1 and S2 were prepared for microstructural characterization by mechanically polishing to a 0.05 μm finish, followed by etching with a solution of 93% CH_3OH + 5% HNO_3 + 2% HCl, and finished by polishing with colloidal silica in a vibratory polisher for three hours. S3 was similarly prepared, but an etchant of 98% C_2H_5OH + 2% HCl was used instead. Optical microscopy was performed using a Zeiss optical microscope equipped with an Axiocam HRc digital camera, and SEM was performed using an FEI Inspect F SEM. X-ray energy dispersive spectroscopy (XEDS) was performed within the Inspect SEM to identify the chemical composition of intermetallic precipitates. Electron backscatter diffraction (EBSD) was used in conjunction with OM and SEM to help characterize the microstructure of the three solders as well as to provide crystallographic texture information for these materials. EBSD was performed on a Philips XL30 Field Emission Gun SEM equipped with a Hikari high-speed EBSD detector. Data was acquired and analyzed using orientation imaging microscopy (OIM) software by TexSEM Laboratories (TSL) of EDAX.

Mechanical testing in compression was conducted on the three solder materials under quasi-static and dynamic loading conditions. Cylindrical samples 5 mm in diameter and 5 mm in height were machined from the as-received materials with the loading direction of the samples parallel to the longitudinal direction of the as-received solder bars. Quasi-static tests were performed in an Instron load frame at strain rates of 10^{-3}–10^{-1} s^{-1}. Dynamic tests were performed using a Split Hopkinson Pressure Bar (SHPB) apparatus at strain rates of 1250–2700 s^{-1}. In all cases, specimens were tested to strains in excess of 10% to establish the stress–strain curves. These tests were also performed as a function of temperature. The temperature range investigated was −196–60 °C.

To establish the influence of room temperature recovery, two-step quasi-static compression tests at strain rates ranging from 10^{-3} to 10^{-2} s^{-1} were conducted. The two-step process consisted of loading to a strain of 20% and subsequent reloading up to 70% after a set dwell period with no load. Following mechanical deformation, the microstructural changes of the three solder materials were again characterized via OM, SEM, XEDS, and EBSD techniques.

3. Results and discussion

The as-received microstructure for the three alloys, as revealed by OM, is shown in Fig. 1. S1 showed a homogenous microstructure with nominally equiaxed grains in the matrix. The microstructures in both the cross-sectional and longitudinal sections were seen to be fairly uniform and consisted of a Sn and Pb eutectic structure. Sn grains had an average diameter of 6.4 μm, while the Pb grains had an average diameter of 3.7 μm. In Fig. 1, Sn grains appear light and the Pb grains appear dark. S2 was qualitatively more heterogeneous with some strings of Pb grains parallel to the transverse direction. Average grain diameter measured 4.7 μm for the Sn grains and 3.2 μm for the Pb grains. Also observed were occasional Ag_3Sn intermetallic particles, identified as such through SEM XEDS. Fig. 2 shows an SEM image of the S2 microstructure and a corresponding XEDS micrograph displaying the presence of gold from the Ag(L) emission. The Ag_3Sn particles appeared to be aligned with the Pb grains, and the majority of this phase was on the submicron scale, though some larger sized particles were also observed. S3 showed a heterogeneous microstructure in both the cross-sectional and longitudinal directions. Intermetallic precipitates were observed in the as-received microstructure and were heavily aligned along the longitudinal direction, indicating an extruded structure. The compositions of these precipitates were identified as Ag_3Sn and Cu_6Sn_5 by XEDS; Fig. 2 shows the S3 microstructure as well as XEDS micrographs of the Ag(L) and Cu(K) emissions.

Texture analysis was also performed on the as-received S1, S2, and S3 solder alloys using EBSD, as shown in Fig. 3. For all alloys, the texture provided is for the tin phase, as it is the primary constituent within the microstructure. Also, microstructures shown for the S1 and S2 solders have been cleaned via nearest neighbor point correlation with a threshold confidence index of 0.2; noise in the microstructures is from the lead phase, which is difficult to image properly using EBSD. Initially, S1 exhibits a slight [0 1 1] texture while S2 is essentially random. On the other hand, S3 initially possesses a strong [1 0 $\bar{1}$] texture.

Quasi-static compression tests performed at strain rates of 0.001 and 0.1 s^{-1} at room temperature and at liquid nitrogen temperature showed that yield strength increases from S1 to S2 to S3, as shown in the stress–strain plots of Fig. 4. For all the alloys, yield strength increased with increased strain-rate and decreased temperature within the quasi-static strain-rate regime. While work hardening was observed under most conditions, work softening occurred under room temperature, low strain rate (0.001 s^{-1}) conditions for the S1 and S3 alloys. While S1 and S2 possessed qualitatively similar microstructures, the grain size for the as-received S2 was approximately half that of S1 (Fig. 1). In addition, S2 possessed a measurable volume fraction of Ag_3Sn precipitates that were not present in S1, as evidenced by Fig. 2.

The increase in yield strength from S1 to S2 is expected in part due to Hall–Petch strengthening due to reduced grain sizes in S2 [17,18]. In addition, precipitation hardening from Ag_3Sn particles is also expected to contribute to the increased yield strength of S2 over S1 [19]. The further increase in strength of S3 as compared to S1 and S2 can also be partially attributed to Hall–Petch strengthening as well as precipitation hardening from numerous Ag_3Sn and Cu_6Sn_5 rod-like precipitates of less than a micron to 5 μm in size, as shown in Fig. 2. In addition, the comparatively strong [1 0 $\bar{1}$] texture of S3 as compared to the random texture of S1 and S2 likely also contributes to the enhanced strength of S3.

Dynamic compression tests performed at strain rates of 1250–2700 s^{-1} displayed a sensitivity of yield stress to strain rate, with higher yield stresses at higher strain rates, as shown in Fig. 5. In addition, all three alloys displayed increased strength with decreases in temperature. While the difference in the stress–strain relationship between S1 and S2 became less significant at higher strain rates, S3 remained noticeably stronger than the other two alloys. Work hardening rates extracted from roughly 2 to 6% strain for the three test temperatures showed that the work hardening rate appears to be relatively insensitive to temperature changes between 60 °C and 20 °C. However, the work hardening rate was notably higher at −40 °C. For example, the work hardening rate for alloy S2 was calculated at 500 MPa (per unit strain) at 60 °C, 580 MPa at 20 °C, and 840 MPa at −40 °C. This suggests that efficient dynamic recovery occurs at temperatures above 20 °C and that stored defects contribute to work hardening at temperatures below 20 °C.

In addition to quasi-static and dynamic compression tests, two-step compression tests were performed at strain rates of 0.001–0.01 s^{-1} and temperatures of 20 °C to −40 °C. The results of these tests are shown in Fig. 6. While all solders experienced a decrease in flow stress following static aging at 20 °C, negligible decreases in flow stress were observed after a 10 min dwell at −40 °C. In contrast, notable decreases in flow stress occurred in all three solders tested at −40 °C but with a 5 min dwell at room temperature, indicating that the recovery rate in the solders at room temperature is relatively rapid.

In addition to the as-received microstructural characterization, the deformed microstructures for all three solders were also characterized. SEM observations showed that minor grain coarsening occurred with increasing strain in the cross-sectional microstructure of S1, while slightly more pronounced coarsening occurred in the cross-sectional microstructure of S2 with increasing strain, as shown in Fig. 7a and b (as compared to Fig. 3a and b). While coarsening increased with increasing deformation strain, no obvious differences in grain coarsening were observed as a function of strain rate variation for the two leaded solders. Additional experimentation showed that for both S1 and S2, grain coarsening also

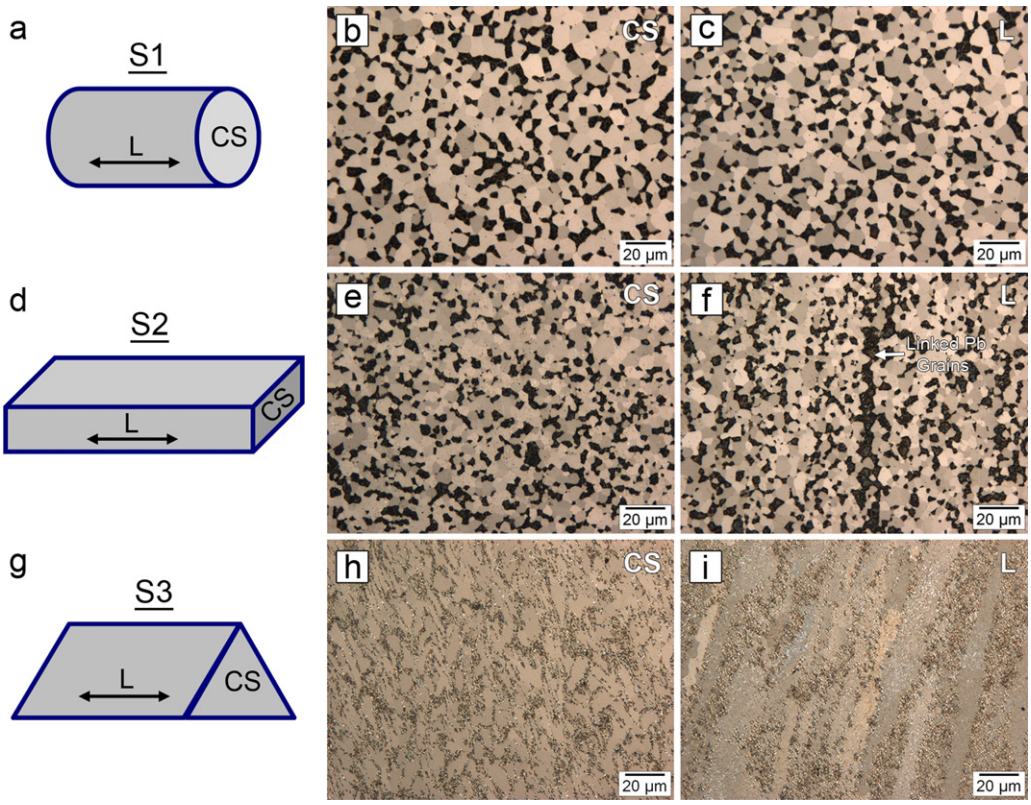

Fig. 1. Solder bar stock schematics with corresponding OM microstructure images of the cross-sectional (CS) and longitudinal (L) sections of the as-received alloys (a, b, c) S1, (d, e, f) S2, and (g, h, i) S3.

occurred at decreased deformation temperature after compression to similar strains in the longitudinal direction, although this change in grain morphology was not as substantial as it was at higher temperatures. In terms of texture evolution, deformed S1 textures did not vary substantially from the undeformed S1 alloy (Fig. 7a). Deformed S2 samples exhibited a very slight evolution of a [0 0 1] texture but overall remained close to random, as in the undeformed S2 alloy (Fig. 7b).

In the case of the S1 and S2 alloys, substantial coarsening of the microstructure as a function of strain was expected to contribute significantly to the work hardening rate as a function of strain. However, while coarsening was not observed to change drastically with strain rate, the work hardening response of the S1 and S2 alloys did change substantially with strain rate, as shown in Fig. 3a and b and Fig. 4a and b. Additionally, in the cases where grain coarsening was not prominently observed, such as at low temperatures, a similar influence of strain rate on work hardening was observed. Specifically, it is observed in Figs. 3 and 4 that work hardening rates increased substantially as a function of strain rate for S1 and S2 at all temperatures investigated in this study. These observations

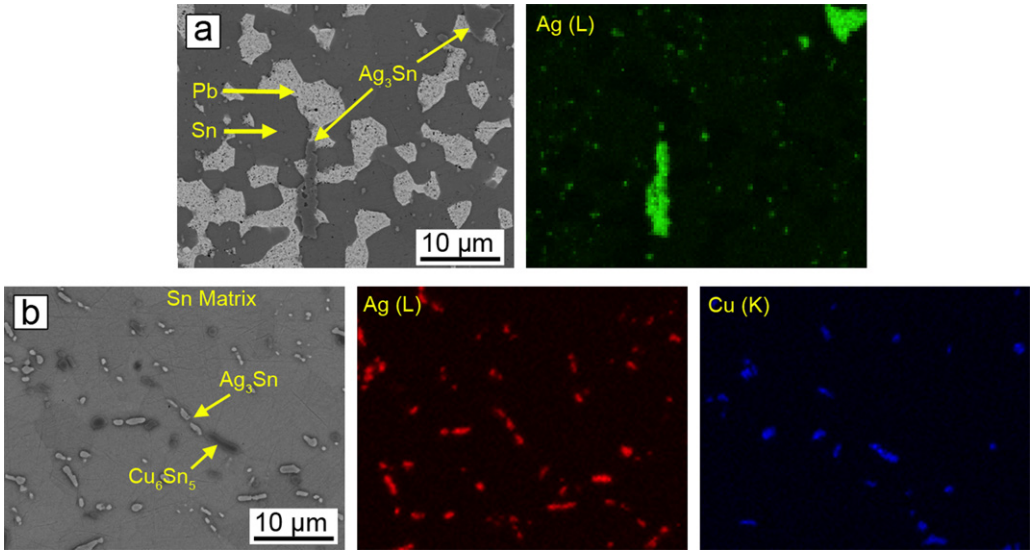

Fig. 2. SEM and XEDS images of (a) Ag_3Sn precipitates in S2 and (b) Ag_3Sn and Cu_6Sn_5 precipitates in S3.

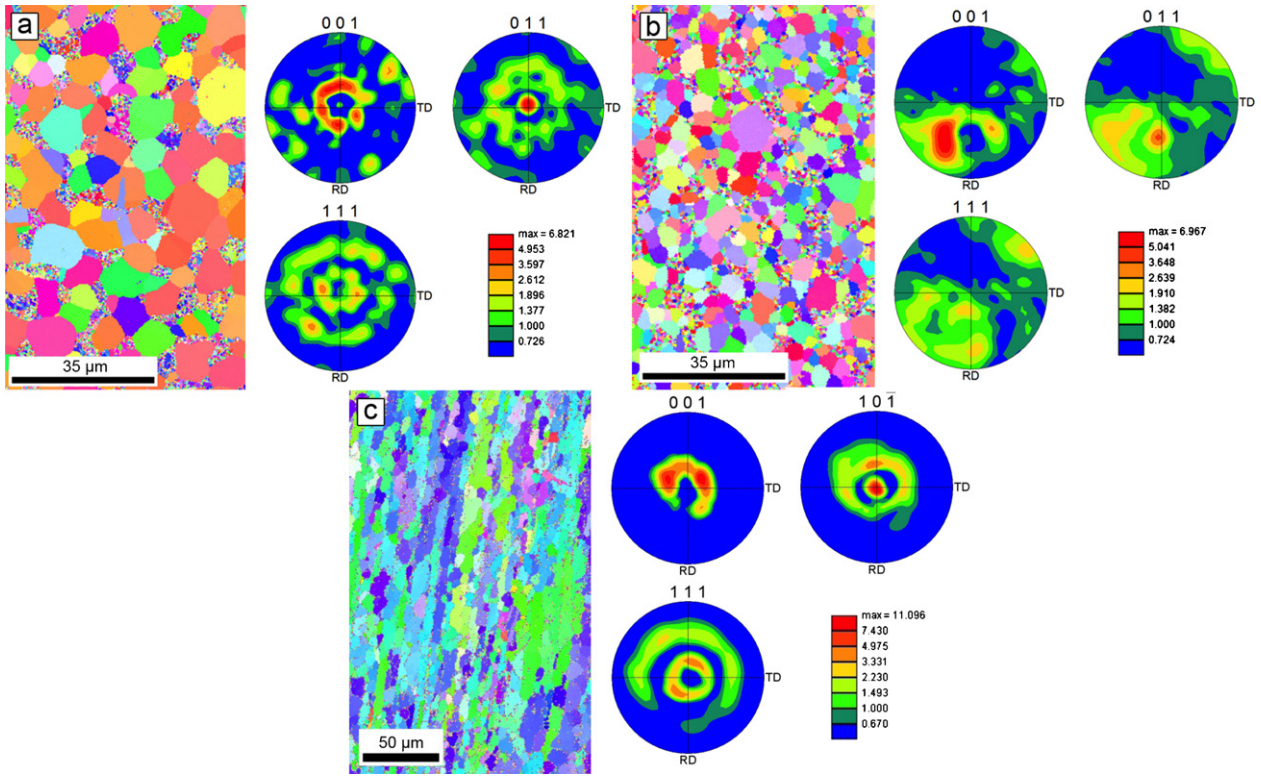

Fig. 3. EBSD inverse pole figure maps and corresponding texture plots for undeformed (a) S1, (b) S2, and (c) S3. While S1 and S2 possess only a slight initial texture, S3 has a strong [1 0 $\bar{1}$] type initial texture.

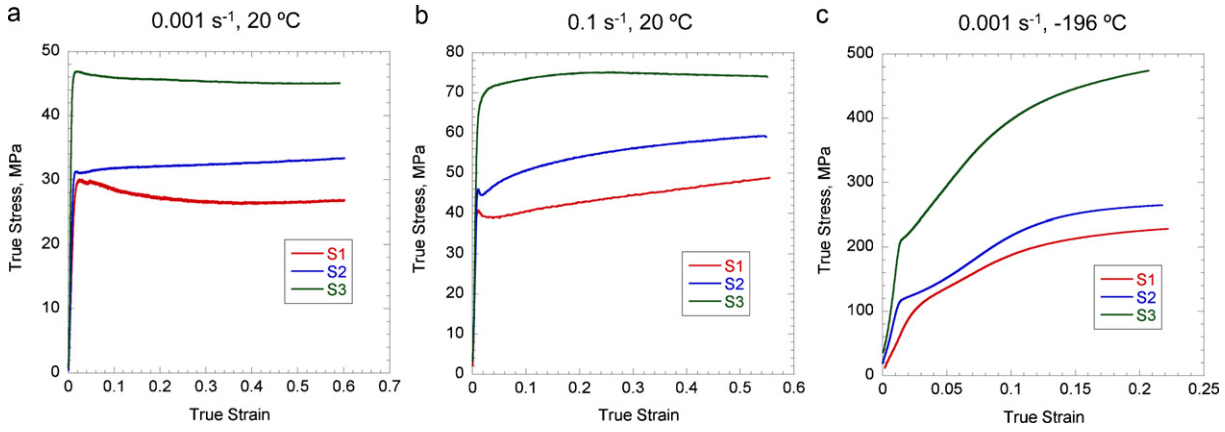

Fig. 4. Stress–strain curves for S1, S2, and S3 under quasi-static compression conditions at 20 °C and −196 °C.

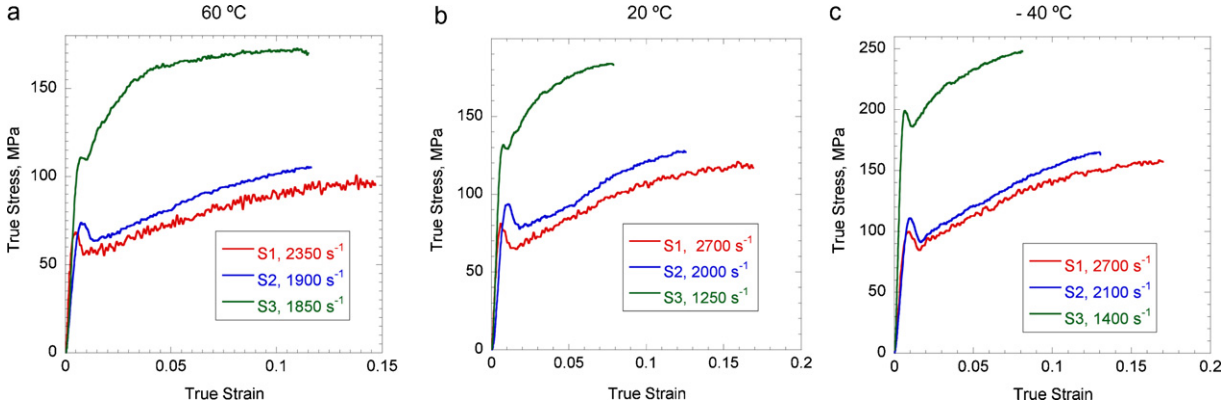

Fig. 5. Stress–strain curves for S1, S2, and S3 under dynamic compression conditions at 60 °C, 20 °C, and −40 °C.

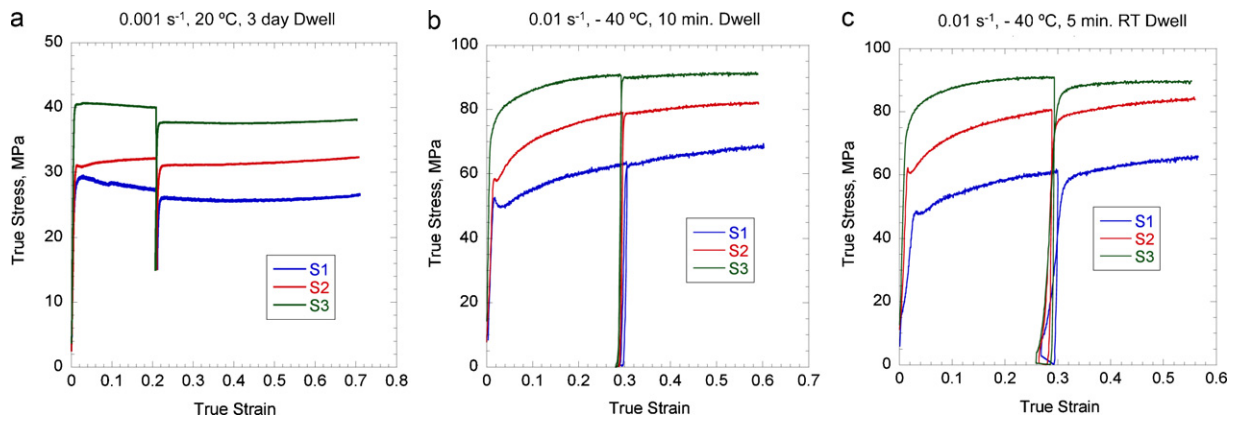

Fig. 6. Stress–strain curves for S1, S2, and S3 undergoing two-step compression tests at strain rates of 0.001–0.01 s^{-1} and temperatures of 20 °C to −40 °C.

suggest that defect generation and storage mechanisms dominate the mechanical response of the S1 and S2 alloys at both quasi-static and dynamic strain rates, at least up to strains of 15%, and that grain coarsening has less of an influence on the mechanical response in this strain regime.

In the case of the S3 alloy, microstructural evolution during deformation was observed to be more significant than in the S1 and S2 cases. Fig. 8 shows EBSD scans of longitudinal sections of S3 in the as-received state as well as after testing at a strain rate 0.001 s^{-1} to 5% and 60% strain at 20 °C and to 20% strain at −196 °C. The as-received material exhibited predominately elongated grains oriented parallel to the longitudinal direction. The grain aspect ratio, defined as the length of the minor axis over the length of the major axis of an ellipse fitted to an individual grain, had a median of 0.27 for as-received S3, indicating highly elongated grains. With increasing deformation at 20 °C, the distribution of the grain aspect ratio shifted higher, such that at 60% strain, the S3 sample possessed a grain aspect ratio with both a mean and median of ∼0.5. Average grain size grew from 5.7 μm to 6.9 μm within the first 5% strain but then dropped to 4.2 μm at 60% strain. The combination of the redistribution of the grain aspect ratio and the drop in grain size suggests that recrystallization occurs in S3 at large strains. Given that efficient dynamic recovery occurs at even moderate temperatures, substantial strain was necessary to cause recrystallization at 20 °C. Compared to the room temperature compression tests, the sample tested at −196 °C exhibited significant grain coarsening at just 20% strain. Based on the mechanical test data and post mortem metallographic analysis of the microstructure, we believe that while significant work hardening occurred in the sample at −196 °C, recrystallization and grain growth occurred after testing while the sample rested at room temperature. In addition, texture analysis of S3 showed that a strong [1 0 $\bar{1}$] fiber texture

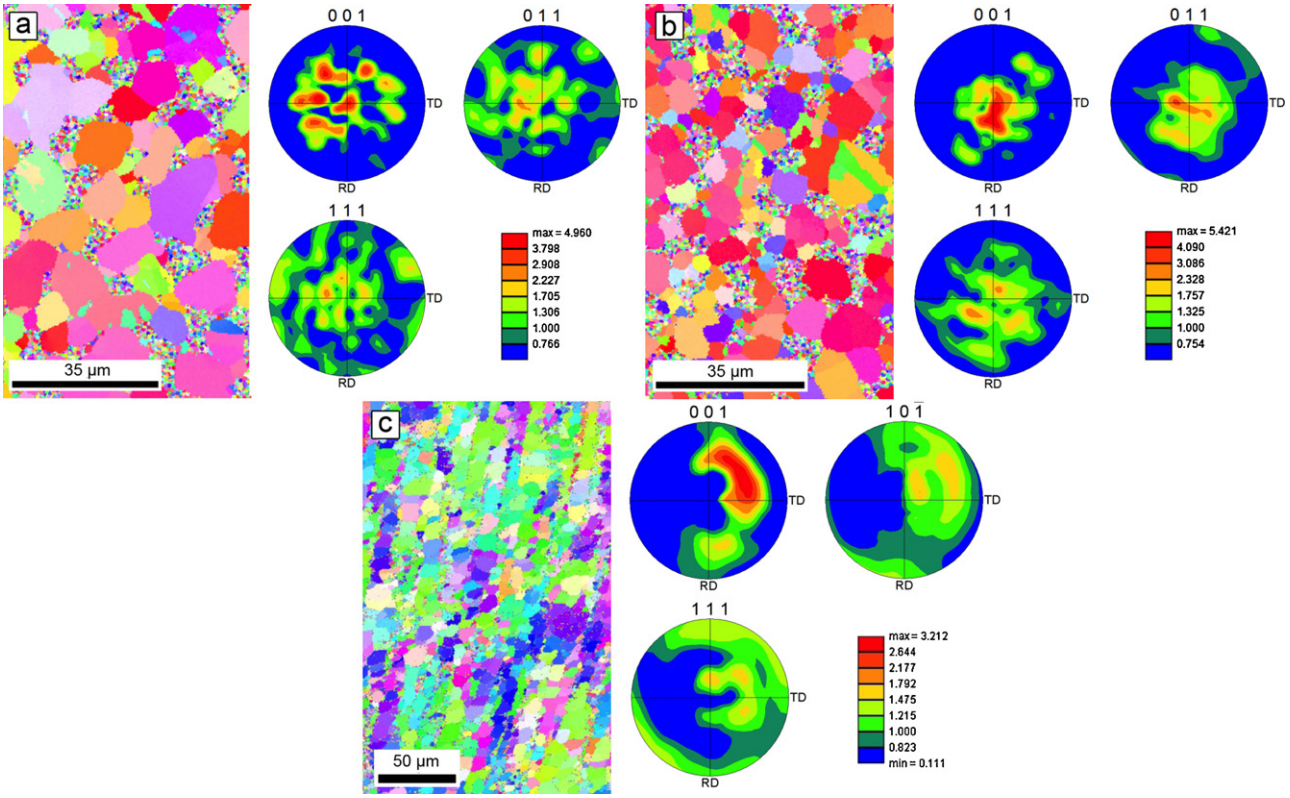

Fig. 7. EBSD inverse pole figure maps and corresponding texture plots for (a) S1 deformed at 20 °C, $\varepsilon = 0.17$, and $\dot{\varepsilon} = 2700\ s^{-1}$, (b) S2 deformed at 20 °C, $\varepsilon = 0.13$, and $\dot{\varepsilon} = 2000\ s^{-1}$, and (c) S3 deformed at 20 °C, $\varepsilon = 0.6$, and $\dot{\varepsilon} = 0.1\ s^{-1}$.

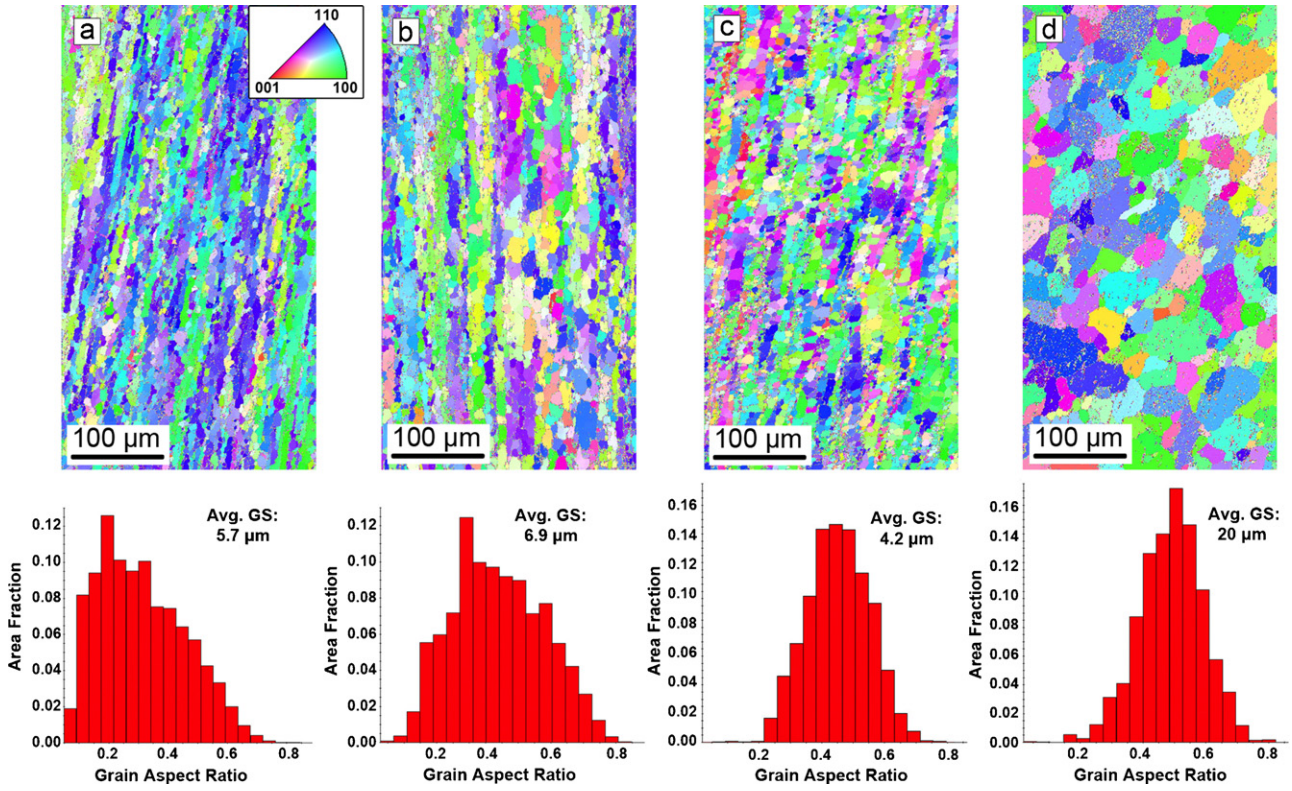

Fig. 8. EBSD scans of S3: (a) as-received, (b) at a strain of ~0.05, and (c) at a strain of ~0.6. Tests were performed at a strain rate of 0.001 s^{-1} at 20 °C, with the exception of (d) which was performed at −196 °C to a strain of ~0.2. An inverse pole figure for the scans is included in (a). Grain aspect ratio plots indicate the elongation of the grains within each sample, with a low aspect ratio indicating greater elongation. Average grain sizes for the different test conditions are also given.

existed in the as-received sample (Fig. 3c) but was weakened by compressive deformation, with the texture weakening increasing with stored work during deformation (Fig. 7c). The combination of grain coarsening and recrystallization leading to texture weakening likely contributes to a significant drop in work hardening rates at strains of only 5% under dynamic loads and 10% under quasi-static loads.

4. Conclusions

The mechanical properties and microstructural characteristics of three solder alloys, Sn63Pb37 (S1), Sn62Pb36Ag2 (S2), and Sn96.5Ag3Cu0.5 (S3) were quantified for a range of strains, strain rates, and temperatures. S1 and S2 exhibited similar responses to one another under all conditions, but overall, S3 possessed the highest yield stress for all the tested strain rates and temperatures. Some degree of work softening was observed in all three solder alloys during deformation at room temperature and low strain rates, but pronounced work hardening was displayed under conditions of low temperature and/or high strain rate. During high strain rate deformation, the work hardening rate was found to be insensitive to deformation at temperatures ≥20 °C, suggesting efficient dynamic recovery at room temperature for all three solders. In terms of microstructural characteristics, both S1 and S2 exhibited grain coarsening with increasing plastic strain and deformation temperature, which led to reduced rates of work hardening at higher strains. In S3, both static recrystallization and grain coarsening occurred with increasing stored work during deformation. In general, Sn96.5Ag3Cu0.5 seems to be a worthy candidate for widespread replacement of leaded solders due to its improved yield stress performance at a variety of strain rates that encompass both thermal stress and drop test conditions.

Acknowledgments

Los Alamos National Laboratory is operated by LANS, LLC, for the National Nuclear Security Administration of the US Department of Energy under contract DE-AC52-06NA25396. This work has been performed under the auspices of the US Department of Energy and supported by the Joint DoD/DoE Munitions Technology Development Program.

References

[1] E.E.d. Kluizenaar, Solder. Surf. Mt. Technol. 2 (1990) 27–38.
[2] K.N. Subramanian, J.G. Lee, Mat. Sci. Eng. A: Struct. 421 (2006) 46–56.
[3] Y.C. Chan, D. Yang, Prog. Mater. Sci. 55 (2010) 428–475.
[4] K.N. Tu, A.M. Gusak, M. Li, J. Appl. Phys. 93 (2003) 1335–1353.
[5] W.H. Muller, Microelectron. Reliab. 44 (2004) 1901–1914.
[6] B. Wang, S. Yi, J. Mater. Sci. Lett. 21 (2002) 697–698.
[7] E.H. Wong, C.S. Selvanayagam, S.K.W. Seah, W.D. Van Driel, J. Caers, X.J. Zhao, N. Owens, L.C. Tan, D.R. Frear, M. Leoni, Y.S. Lai, C.L. Yeh, J. Electron. Mater. 37 (2008) 829–836.
[8] M. Amagai, M. Watanabe, M. Omiya, K. Kishimoto, T. Shibuya, Microelectron. Reliab. 42 (2002) 951–966.
[9] C.R. Siviour, S.M. Walley, W.G. Proud, J.E. Field, J. Phys. D: Appl. Phys. 38 (2005) 4131–4139.
[10] J. Shen, Y.C. Chan, J. Alloys Compd. 477 (2009) 552–559.
[11] R. Darveaux, K. Banerji, IEEE T. Compon. Hybr. 15 (1992) 1013–1024.
[12] F.L. Zhu, H.H. Zhang, R.F. Guan, S. Liu, J. Alloys Compd. 438 (2007) 100–105.
[13] R.S. Sidhu, N. Chawla, Metall. Mater. Trans. A 39A (2008) 340–348.
[14] A.K. Gain, T. Fouzder, Y.C. Chan, A. Sharif, W.K.C. Yung, J. Alloys Compd. 489 (2010) 678–684.
[15] C.A. Harper, Electronic Materials and Processes Handbook, McGraw-Hill, USA, 2004.
[16] BALVER ZINN SOLDER SN97C (SnAg3.0Cu0.5), in: Technical Data Sheet, Balve, Germany, 2007.
[17] E.O. Hall, P. Phys. Soc. Lond. B 64 (1951) 747–753.
[18] N.J. Petch, J. Iron Steel I. 174 (1953) 25–28.
[19] A. Kelly, R.B. Nicholson, Prog. Mater. Sci. 10 (1963) 151–391.